INTERNATIONAL JOURNAL FOR NUMERICAL METHODS IN FLUIDS
Int. J. Numer. Meth. Fluids (2008)
Published online in Wiley InterScience (www.interscience.wiley.com). DOI: 10.1002/fld.1952

Depth-integrated, non-hydrostatic model for wave breaking and run-up

Yoshiki Yamazaki[1], Zygmunt Kowalik[2] and Kwok Fai Cheung[1,*,†]

[1]*Department of Ocean and Resources Engineering, University of Hawaii at Manoa, Honolulu, HI 96822, U.S.A.*
[2]*Institute of Marine Science, University of Alaska, Fairbanks, AK 99775, U.S.A.*

SUMMARY

This paper describes the formulation, verification, and validation of a depth-integrated, non-hydrostatic model with a semi-implicit, finite difference scheme. The formulation builds on the nonlinear shallow-water equations and utilizes a non-hydrostatic pressure term to describe weakly dispersive waves. A momentum-conserved advection scheme enables modeling of breaking waves without the aid of analytical solutions for bore approximation or empirical equations for energy dissipation. An upwind scheme extrapolates the free-surface elevation instead of the flow depth to provide the flux in the momentum and continuity equations. This greatly improves the model stability, which is essential for computation of energetic breaking waves and run-up. The computed results show very good agreement with laboratory data for wave propagation, transformation, breaking, and run-up. Since the numerical scheme to the momentum and continuity equations remains explicit, the implicit non-hydrostatic solution is directly applicable to existing nonlinear shallow-water models. Copyright © 2008 John Wiley & Sons, Ltd.

Received 27 March 2008; Revised 3 September 2008; Accepted 23 September 2008

KEY WORDS: non-hydrostatic; dispersive waves; upwind flux approximation; momentum-conserved advection; breaking waves; run-up

1. INTRODUCTION

The nonlinear shallow-water equations have many applications in modeling of long waves such as tides, storm surges, and tsunamis. The finite difference method, owing to its simplicity in formulation and ease of implementation, is widely used in the solution schemes of the depth-integrated

*Correspondence to: Kwok Fai Cheung, Department of Ocean and Resources Engineering, University of Hawaii at Manoa, HI 96822, U.S.A.
†E-mail: cheung@hawaii.edu

Contract/grant sponsor: University of Hawaii Sea Grant College Program; contract/grant number: NA05OAR4171048
Contract/grant sponsor: National Tsunami Hazard Mitigation Program
Contract/grant sponsor: Hawaii State Civil Defense

governing equations. Researchers have made significant efforts in improving numerical schemes and boundary treatments to model long-wave propagation, transformation, and run-up [1–6]. These explicit schemes provide efficient solutions for large computational problems, thereby enabling their extensive application in modeling of tsunamis and the associated flood hazards. Despite the advancements, the issues with wave breaking and dispersion remain unresolved with these finite difference models.

The commonly used finite difference schemes for the nonlinear shallow-water equations are non-conservative; this results in volume loss and energy dissipation as the wave steepness increases and the flow approaches discontinuity. This becomes an important modeling issue when tsunami or tidal bores develop near shore. Some models remain stable after wave breaking leading to the convenient assertion that these models mimic the energy loss with numerical dissipation, even though the dissipation itself is grid dependent. Stelling and Duinmeijer [7] developed a conservative formulation of the advective terms in the momentum equations to handle flow discontinuity for velocity-based nonlinear shallow-water models. They impose energy conservation to strong flow contractions and momentum conservation to mild flow contractions and expansions. Their approach approximates flow discontinuities as bores or hydraulic jumps as in a finite volume model, using a Riemann solver [8–10].

Horrillo *et al.* [11] showed that the lack of dispersion in shallow-water models results in underestimation of far-field tsunami impacts. Stelling and Zijlema [12] proposed a semi-implicit finite difference model, which accounts for dispersion through a non-hydrostatic pressure term. In both the depth-integrated and multi-layer formulations, they decompose the pressure into hydrostatic and non-hydrostatic components as in Casulli [13] and apply the Keller-box scheme [14] in the vertical gradient approximation of the non-hydrostatic pressure. The solution to the hydrostatic problem remains explicit; the non-hydrostatic solution derives from an implicit scheme to the three-dimensional continuity equation. The depth-integrated governing equations are relatively simple and analogous to the nonlinear shallow-water equations with the addition of a vertical momentum equation and non-hydrostatic terms in the horizontal momentum equations. Walters [15] adapted this non-hydrostatic approach into a finite element method. Numerical results show that both depth-integrated models estimate the dispersive waves slightly better than the classical Boussinesq equations of Peregrine [16].

Zijlema and Stelling [17] recently extended their multi-layer model to include the momentum-conserved formulation for the advective terms and an upwind approximation in the continuity equation, and derived semi-implicit schemes for both the hydrostatic and non-hydrostatic solutions. Their two-layer model can handle wave breaking without the use of empirical relations for energy dissipation and provide comparable results with those of extended Boussinesq models [18–20]. Such a non-hydrostatic approach, if builds on existing nonlinear shallow-water models with explicit schemes [1–6], will have greater application in the research community. Stability, however, is a critical issue. The difficulty lies in the flux approximation, in which the velocity and flow depth are evaluated at different locations in a finite difference scheme. The resulting errors in flux estimations often become the source of instability. Mader [21] proposed a unique upwind scheme that extrapolates the surface elevation instead of the flow depth to determine explicitly the flux in the continuity equation of a nonlinear shallow-water model. Kowalik *et al.* [22] implemented this upwind flux approximation and showed remarkable stability in simulating global tsunami propagation and run-up.

In this paper, we propose a depth-integrated non-hydrostatic model capable of handling flow discontinuities associated with breaking waves and hydraulic jumps. The present formulation,

DOI: 10.1002/fld

which builds on an explicit scheme of the nonlinear shallow-water equations, allows a direct implementation of the upwind flux approximation of Kowalik *et al.* [22] to improve model stability for discontinuous flows. Simulation of solitary wave propagation and sinusoidal wave transformation over a submerged bar provides validation of the dispersion characteristics of the proposed non-hydrostatic model. Solitary wave transformation over a plane beach and a conical island provides a series of validation tests for modeling of wave breaking and run-up. These near shore processes including energetic breaking waves have been used extensively for validation of nonlinear shallow-water and Boussinesq-type models, but examinations of depth-integrated non-hydrostatic models in describing these processes are less immediately evident. The modular structure of the proposed non-hydrostatic model allows a systematic examination of the numerical characteristics by turning the momentum-conserved advection and upwind flux approximation on and off in the tests.

2. GOVERNING EQUATIONS

In this section, we summarize the formulation and assumptions of the governing equations for the depth-integrated, non-hydrostatic free-surface flow. The governing equations are derived from the incompressible Navier–Stokes equations and the continuity equation in the Cartesian coordinates system (x, y, z) given as

$$\frac{\partial u}{\partial t}+u\frac{\partial u}{\partial x}+v\frac{\partial u}{\partial y}+w\frac{\partial u}{\partial z}=-\frac{1}{\rho}\frac{\partial p}{\partial x}+\nu\left(\frac{\partial^2 u}{\partial x^2}+\frac{\partial^2 u}{\partial y^2}+\frac{\partial^2 u}{\partial z^2}\right) \tag{1}$$

$$\frac{\partial v}{\partial t}+u\frac{\partial v}{\partial x}+v\frac{\partial v}{\partial y}+w\frac{\partial v}{\partial z}=-\frac{1}{\rho}\frac{\partial p}{\partial y}+\nu\left(\frac{\partial^2 v}{\partial x^2}+\frac{\partial^2 v}{\partial y^2}+\frac{\partial^2 v}{\partial z^2}\right) \tag{2}$$

$$\frac{\partial w}{\partial t}+u\frac{\partial w}{\partial x}+v\frac{\partial w}{\partial y}+w\frac{\partial w}{\partial z}=-\frac{1}{\rho}\frac{\partial p}{\partial z}+\nu\left(\frac{\partial^2 w}{\partial x^2}+\frac{\partial^2 w}{\partial y^2}+\frac{\partial^2 w}{\partial z^2}\right)-g \tag{3}$$

$$\frac{\partial u}{\partial x}+\frac{\partial v}{\partial y}+\frac{\partial w}{\partial z}=0 \tag{4}$$

where (u, v, w) is flow velocity; t is time, ρ is water density; p is pressure; g is gravitational acceleration; and ν is the kinematic viscosity coefficient.

The flow depth is defined as $D=\zeta+h$ where ζ is the surface elevation measured from the still-water level and h is the water depth. Material derivatives of the surface elevation and water depth give rise to the kinematic free surface and seabed boundary conditions as

$$w=\frac{D(\zeta)}{Dt}=\frac{\partial \zeta}{\partial t}+u\frac{\partial \zeta}{\partial x}+v\frac{\partial \zeta}{\partial y} \quad \text{at } z=\zeta \tag{5}$$

$$w=\frac{D(-h)}{Dt}=-u\frac{\partial h}{\partial x}-v\frac{\partial h}{\partial y} \quad \text{at } z=-h \tag{6}$$

The vertical velocity w varies linearly from the seabed to the free surface for modeling of weakly dispersive waves in depth-integrated flows. The vertical advective and dissipative terms, which

DOI: 10.1002/fld

are small compared with their horizontal counterparts, can consistently be omitted in the vertical momentum equation (3). Following Stelling and Zijlema [12] and Casulli [13], we decompose the pressure into hydrostatic and non-hydrostatic components as

$$p=\rho g(\zeta-z)+q \tag{7}$$

where q denotes the non-hydrostatic pressure. Both the hydrostatic and non-hydrostatic pressure terms vanish at $z=\zeta$ to provide the dynamic free-surface boundary condition.

Depth integration of (1), (2), and (4) and linearization of (3) with the Keller-box scheme [14], taking into account the boundary conditions (5) and (6) and the pressure decomposition (7), yield the governing equations of the non-hydrostatic free-surface flow [12]. The resulting x, y, and z momentum equations as well as the continuity equation are

$$\frac{\partial U}{\partial t}+U\frac{\partial U}{\partial x}+V\frac{\partial U}{\partial y}=-g\frac{\partial \zeta}{\partial x}-\frac{1}{2}\frac{1}{\rho}\frac{\partial q}{\partial x}-\frac{1}{2}\frac{q}{D\rho}\frac{\partial}{\partial x}(\zeta-h)-n^2\frac{g}{D^{1/3}}\frac{U\sqrt{U^2+V^2}}{\rho D} \tag{8}$$

$$\frac{\partial V}{\partial t}+U\frac{\partial V}{\partial x}+V\frac{\partial V}{\partial y}=-g\frac{\partial \zeta}{\partial y}-\frac{1}{2}\frac{1}{\rho}\frac{\partial q}{\partial y}-\frac{1}{2}\frac{q}{D\rho}\frac{\partial}{\partial y}(\zeta-h)-n^2\frac{g}{D^{1/3}}\frac{V\sqrt{U^2+V^2}}{\rho D} \tag{9}$$

$$\frac{\partial W}{\partial t}=\frac{q}{\rho D} \tag{10}$$

$$\frac{\partial \zeta}{\partial t}+\frac{\partial (UD)}{\partial x}+\frac{\partial (VD)}{\partial y}=0 \tag{11}$$

where U, V, and W are depth-averaged velocity components in the x, y, and z directions; q is now defined as the non-hydrostatic pressure at the bottom; and n is Manning's roughness coefficient. Because of the assumption of a linear distribution for w, the velocity component W is simply the average value of w at the free surface and the seabed given, respectively in (5) and (6). Except for the addition of the vertical momentum equation and the non-hydrostatic pressure in the horizontal momentum equations, the governing equations have the same structure as the nonlinear shallow-water equations. This formulation allows a straightforward extension of existing nonlinear shallow-water models for non-hydrostatic flows.

3. NUMERICAL FORMULATION

The numerical formulation includes the solution schemes for the hydrostatic and non-hydrostatic components of the governing equations as well as the treatment of the moving waterline for run-up calculation. The finite difference scheme utilizes the upwind flux approximation of Kowalik *et al.* [22] in the continuity equation as well as the calculation of the advective terms in the horizontal momentum equations. Figure 1 shows the space-staggered grid for the computation. The model calculates the horizontal velocity components U and V at the cell interface and the free-surface elevation ζ, the non-hydrostatic pressure q, and the vertical velocity W at the cell center, where the water depth h is defined.

DOI: 10.1002/fld

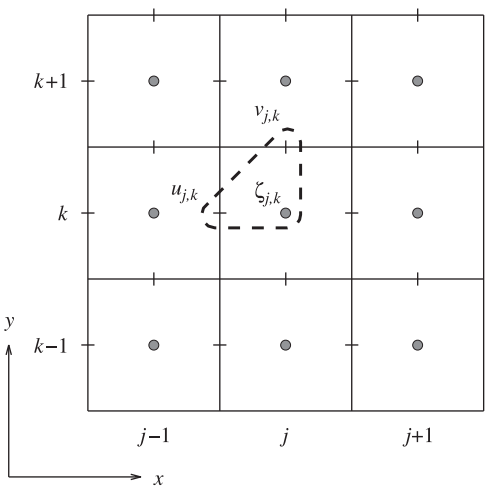

Figure 1. Definition sketch of spatial grid.

3.1. Hydrostatic model

The hydrostatic model utilizes an explicit scheme for the solution. Integration of the continuity equation (11) provides an update of the surface elevation at the center of cell (j,k) in terms of the x and y fluxes, FLX and FLY, at the cell interfaces as

$$\zeta_{j,k}^{m+1}=\zeta_{j,k}^{m}-\Delta t\frac{(\mathrm{FLX}_{j+1,k}-\mathrm{FLX}_{j,k})}{\Delta x}-\Delta t\frac{(\mathrm{FLY}_{j,k}-\mathrm{FLY}_{j,k-1})}{\Delta y} \tag{12}$$

where m denotes the time step, Δt the time step size, and Δx and Δy the grid sizes in the x and y directions. The upwind scheme gives the flux terms at (j,k) as

$$\mathrm{FLX}_{j,k}=U_p^{m+1}\zeta_{j-1,k}^{m}+U_n^{m+1}\zeta_{j,k}^{m}+U_{j,k}^{m+1}\frac{(h_{j-1,k}+h_{j,k})}{2} \tag{13a}$$

$$\mathrm{FLY}_{j,k}=V_p^{m+1}\zeta_{j,k}^{m}+V_n^{m+1}\zeta_{j,k+1}^{m}+V_{j,k}^{m+1}\frac{(h_{j,k}+h_{j,k+1})}{2} \tag{13b}$$

in which

$$U_p^m=\frac{U_{j,k}^m+|U_{j,k}^m|}{2},\quad U_n^m=\frac{U_{j,k}^m-|U_{j,k}^m|}{2},\quad V_p^m=\frac{V_{j,k}^m+|V_{j,k}^m|}{2},\quad V_n^m=\frac{V_{j,k}^m-|V_{j,k}^m|}{2} \tag{14}$$

The upwind flux approximation (13a and 13b) extrapolates the surface elevation from the upwind cell, while the water depth takes on the average value from the two adjacent cells [22]. This represents a departure from most existing shallow-water models [1, 3–6]. Alternatively, the flux can be determined with a second-order scheme as

$$\mathrm{FLX}_{j,k}=U_{j,k}^{m+1}\frac{(\zeta_{j-1,k}^{m}+h_{j-1,k})+(\zeta_{j,k}^{m}+h_{j,k})}{2} \tag{15a}$$

$$\mathrm{FLY}_{j,k}=V_{j,k}^{m+1}\frac{(\zeta_{j,k}^{m}+h_{j,k})+(\zeta_{j,k+1}^{m}+h_{j,k+1})}{2} \tag{15b}$$

DOI: 10.1002/fld

This approach uses average values of the surface elevations and water depths from adjacent cells to determine the flux and is equivalent to the flux-based formulation of the nonlinear shallow-water equations [1, 4, 5].

The horizontal momentum equations provide the velocity components U and V at $(m+1)$ in (13a and 13b) for the update of the surface elevation in (12). In the spatial discretization, the average values of U and V are used in the y- and x-momentum equations, respectively. These average velocity components are defined by

$$\bar{U}^m_{y_{j,k}} = \tfrac{1}{4}(U^m_{j,k} + U^m_{j+1,k} + U^m_{j+1,k+1} + U^m_{j,k+1}) \tag{16}$$

$$\bar{V}^m_{x_{j,k}} = \tfrac{1}{4}(V^m_{j,k} + V^m_{j-1,k} + V^m_{j-1,k-1} + V^m_{j,k-1}) \tag{17}$$

Integration of the x- and y-momentum equations (8) and (9), with the non-hydrostatic terms omitted, provides an intermediate solution for the horizontal velocity

$$\tilde{U}^{m+1}_{j,k} = U^m_{j,k} - \frac{g\Delta t}{\Delta x}(\zeta^m_{j,k} - \zeta^m_{j-1,k}) - \frac{\Delta t}{\Delta x}U^m_p(U^m_{j,k} - U^m_{j-1,k}) - \frac{\Delta t}{\Delta x}U^m_n(U^m_{j+1,k} - U^m_{j,k})$$
$$- \frac{\Delta t}{\Delta y}\bar{V}^m_{x_p}(U^m_{j,k} - U^m_{j,k-1}) - \frac{\Delta t}{\Delta y}\bar{V}^m_{x_n}(U^m_{j,k+1} - U^m_{j,k}) - n^2 g \frac{\Delta t U^m_{j,k}\sqrt{(U^m_{j,k})^2 + (\bar{V}^m_{x_{j,k}})^2}}{(D^m_{j-1,k} + D^m_{j,k})^{4/3}} \tag{18}$$

$$\tilde{V}^{m+1}_{j,k} = V^m_{j,k} - \frac{g\Delta t}{\Delta y}(\zeta^m_{j,k+1} - \zeta^m_{j,k}) - \frac{\Delta t}{\Delta x}\bar{U}^m_{y_p}(V^m_{j,k} - V^m_{j-1,k}) - \frac{\Delta t}{\Delta x}\bar{U}^m_{y_n}(V^m_{j+1,k} - V^m_{j,k})$$
$$- \frac{\Delta t}{\Delta y}V^m_p(V^m_{j,k} - V^m_{j,k-1}) - \frac{\Delta t}{\Delta y}V^m_n(V^m_{j,k+1} - V^m_{j,k}) - n^2 g \frac{\Delta t V^m_{j,k}\sqrt{(\bar{U}^m_{y_{j,k}})^2 + (V^m_{j,k})^2}}{(D^m_{j,k} + D^m_{j,k+1})^{4/3}} \tag{19}$$

where $\bar{V}^m_{xp}$, $\bar{V}^m_{xn}$, $\bar{U}^m_{yp}$, and $\bar{U}^m_{yn}$ are advective speeds in the respective x- and y-momentum equations calculated from (16) and (17).

Most nonlinear shallow-water models, which use the advective speeds from (14) in the momentum equations, cannot capture flow discontinuities associated with breaking waves or hydraulic jumps. Stelling and Duinmeijer [7] derived an alternative discretization of the advective speeds that conserves energy or momentum across flow discontinuities. Momentum conservation provides a better description of bores or hydraulic jumps that mimic breaking waves in depth-integrated flows. We adapt the momentum-conserved advection scheme from [7] with the present upwind flux approximation to provide the advective speeds in the momentum equations. This approach gives rise to U^m_p and U^m_n in the x direction as

$$U^m_p = \frac{\hat{U}^m_{p_{j,k}} + |\hat{U}^m_{p_{j,k}}|}{2}, \quad U^m_n = \frac{\hat{U}^m_{n_{j,k}} - |\hat{U}^m_{n_{j,k}}|}{2} \tag{20}$$

in which

$$\hat{U}^m_{p_{j,k}} = \frac{2\mathrm{FLU}^m_{p\,j,k}}{D^m_{j-1,k} + D^m_{j,k}}, \quad \hat{U}^m_{n_{j,k}} = \frac{2\mathrm{FLU}^m_{n\,j,k}}{D^m_{j-1,k} + D^m_{j,k}} \tag{21}$$

DOI: 10.1002/fld

where the flux for a positive flow ($U^m_{j,k}>0$) is given by

$$\mathrm{FLU}^m_{p\,j,k}=\begin{cases}\dfrac{U^m_{j-1,k}+U^m_{j,k}}{2}\left(h_{j-1,k}+\dfrac{\zeta^m_{j-2,k}+\zeta^m_{j-1,k}}{2}\right) & \text{if } U^m_{j-1,k}>0\\ \dfrac{U^m_{j-1,k}+U^m_{j,k}}{2}(h_{j-1,k}+\zeta^m_{j-1,k}) & \text{if } U^m_{j-1,k}\leqslant 0\end{cases} \tag{22a}$$

and the flux for a negative flow ($U^m_{j,k}<0$) is

$$\mathrm{FLU}^m_{n\,j,k}=\begin{cases}\dfrac{U^m_{j,k}+U^m_{j+1,k}}{2}\left(h_{j,k}+\dfrac{\zeta^m_{j,k}+\zeta^m_{j+1,k}}{2}\right) & \text{if } U^m_{j+1,k}<0\\ \dfrac{U^m_{j,k}+U^m_{j+1,k}}{2}(h_{j,k}+\zeta^m_{j,k}) & \text{if } U^m_{j+1,k}\geqslant 0\end{cases} \tag{22b}$$

Similarly, the momentum-conserved advection scheme modified by the present upwind flux approximation provides the advective speeds V^m_p and V^m_n in the y direction as

$$V^m_p=\frac{\hat{V}^m_{p_{j,k}}+|\hat{V}^m_{p_{j,k}}|}{2},\quad V^m_n=\frac{\hat{V}^m_{n_{j,k}}-|\hat{V}^m_{n_{j,k}}|}{2} \tag{23}$$

in which

$$\hat{V}^m_{p_{j,k}}=\frac{2\mathrm{FLV}^m_{p\,j,k}}{D^m_{j,k}+D^m_{j,k+1}},\quad \hat{V}^m_{n_{j,k}}=\frac{2\mathrm{FLV}^m_{n\,j,k}}{D^m_{j,k}+D^m_{j,k+1}} \tag{24}$$

where

$$\mathrm{FLV}^m_{p\,j,k}=\begin{cases}\dfrac{V^m_{j,k-1}+V^m_{j,k}}{2}\left(h_{j,k}+\dfrac{\zeta^m_{j,k-1}+\zeta^m_{j,k}}{2}\right) & \text{if } V^m_{j,k-1}>0\\ \dfrac{V^m_{j,k-1}+V^m_{j,k}}{2}(h_{j,k}+\zeta^m_{j,k}) & \text{if } V^m_{j,k-1}\leqslant 0\end{cases} \tag{25a}$$

$$\mathrm{FLV}^m_{n\,j,k}=\begin{cases}\dfrac{V^m_{j,k}+V^m_{j,k+1}}{2}\left(h_{j,k+1}+\dfrac{\zeta^m_{j,k+1}+\zeta^m_{j,k+2}}{2}\right) & \text{if } V^m_{j,k+1}<0\\ \dfrac{V^m_{j,k}+V^m_{j,k+1}}{2}(h_{j,k+1}+\zeta^m_{j,k+1}) & \text{if } V^m_{j,k+1}\geqslant 0\end{cases} \tag{25b}$$

The advective speeds $\bar{U}^m_{yp}$, $\bar{U}^m_{yn}$, $\bar{V}^m_{xp}$, and $\bar{V}^m_{xn}$ in (18) and (19) can be obtained from (20) to (25a and 25b) with (16) and (17) as well as average values of $\zeta_{j,k}$, and $h_{j,k}$ calculated in the same way. This completes the numerical formulation for the nonlinear shallow-water equations in describing hydrostatic flows.

In comparison, Stelling and Duinmeijer [7] derived the momentum-conserved advection scheme from the conservative form of the nonlinear shallow-water equations. The resulting momentum equations are the same as the non-conservative form with the exception of the advective speeds,

DOI: 10.1002/fld

which are given by

$$\hat{U}^m_{p_{j,k}} = \frac{2\overline{\mathrm{FLU}}^m_{j-1,k}}{D^m_{j-1,k}+D^m_{j,k}}, \quad \hat{U}^m_{n_{j,k}} = \frac{2\overline{\mathrm{FLU}}^m_{j,k}}{D^m_{j-1,k}+D^m_{j,k}} \tag{26}$$

in which the flux at the cell center is obtained from

$$\overline{\mathrm{FLU}}^m_{j,k} = \frac{\mathrm{FLU}^m_{j,k}+\mathrm{FLU}^m_{j+1,k}}{2} \tag{27}$$

where

$$\mathrm{FLU}^m_{j,k} = \begin{cases} U^m_{j,k} D^m_{j-1,k} & \text{for } U^m_{j,k}>0 \\ U^m_{j,k} D^m_{j,k} & \text{for } U^m_{j,k}<0 \\ U^m_{j,k}[\min(\zeta^m_{j-1,k}, \zeta^m_{j,k})+\max(h_{j-1,k}, h_{j,k})] & \text{for } U^m_{j,k}=0 \end{cases} \tag{28}$$

Note that the averaged fluxes $\overline{\mathrm{FLU}}^m_{j-1,k}$ and $\overline{\mathrm{FLU}}^m_{j,k}$ in (26) are equivalent to $\mathrm{FLU}^m_{pj,k}$ and $\mathrm{FLU}^m_{nj,k}$ in (21) of the present scheme. Their upwind scheme (28) extrapolates the flow depth and calculates the average flux $\overline{\mathrm{FLU}}^m_{j,k}$ at the cell center from the interface values through (27). In contrast, the present approach extrapolates the surface elevation at the cell interface and directly calculates the fluxes $\mathrm{FLU}^m_{p\,j,k}$ and $\mathrm{FLU}^m_{nj,k}$ at the cell center from (22a) and (22b). With the water depth defined at the cell center, any discontinuity is due entirely to the surface elevation. The present upwind scheme avoids errors from depth extrapolation and most importantly improves the capability to capture flow discontinuities. This becomes essential when the topography is irregular and wave breaking is energetic.

3.2. Non-hydrostatic model

This section describes the development of the non-hydrostatic solution from the nonlinear shallow-water results as well as the bottom pressure and vertical velocity terms neglected in the hydrostatic formulation. Integration of the non-hydrostatic terms in the horizontal momentum equations completes the update of the horizontal velocity from (18) and (19)

$$U^{m+1}_{j,k} = \tilde{U}^{m+1}_{j,k} - \frac{\Delta t}{\rho \Delta x} A_{j,k} \frac{(q^{m+1}_{j,k}+q^{m+1}_{j-1,k})}{2} - \frac{\Delta t}{\rho \Delta x} \frac{(q^{m+1}_{j,k}-q^{m+1}_{j-1,k})}{2} \tag{29}$$

$$V^{m+1}_{j,k} = \tilde{V}^{m+1}_{j,k} - \frac{\Delta t}{\rho \Delta y} B_{j,k} \frac{(q^{m+1}_{j,k+1}+q^{m+1}_{j,k})}{2} - \frac{\Delta t}{\rho \Delta y} \frac{(q^{m+1}_{j,k+1}-q^{m+1}_{j,k})}{2} \tag{30}$$

where

$$A_{j,k} = \frac{(\zeta^m_{j,k}-h_{j,k})-(\zeta^m_{j-1,k}-h_{j-1,k})}{(D^m_{j,k}+D^m_{j-1,k})}, \quad B_{j,k} = \frac{(\zeta^m_{j,k+1}-h_{j,k+1})-(\zeta^m_{j,k}-h_{j,k})}{(D^m_{j,k}+D^m_{j,k+1})} \tag{31}$$

Discretization of the vertical momentum equation (10) gives the vertical velocity at the free surface as

$$w^{m+1}_{s_{j,k}} = w^m_{s_{j,k}} - (w^{m+1}_{b_{j,k}} - w^m_{b_{j,k}}) + \frac{2\Delta t}{\rho D^m_{j,k}} q^{m+1}_{j,k} \tag{32}$$

DOI: 10.1002/fld

The vertical velocity at the sea bottom is evaluated from the boundary condition (6) as

$$w_{b_{j,k}}^{m+1} = -\bar{U}_{z_p}^m \frac{h_{j,k} - h_{j-1,k}}{\Delta x} - \bar{U}_{z_n}^m \frac{h_{j+1,k} - h_{j,k}}{\Delta x} - \bar{V}_{z_p}^m \frac{h_{j,k} - h_{j,k-1}}{\Delta y} - \bar{V}_{z_n}^m \frac{h_{j,k+1} - h_{j,k}}{\Delta y} \tag{33}$$

in which

$$\bar{U}_{z_p}^m = \frac{\bar{U}_{z_{j,k}}^m + |\bar{U}_{z_{j,k}}^m|}{2}, \quad \bar{U}_{z_n}^m = \frac{\bar{U}_{z_{j,k}}^m - |\bar{U}_{z_{j,k}}^m|}{2}, \quad \bar{V}_{z_p}^m = \frac{\bar{V}_{z_{j,k}}^m + |\bar{V}_{z_{j,k}}^m|}{2}, \quad \bar{V}_{z_n}^m = \frac{\bar{V}_{z_{j,k}}^m - \bar{V}_{z_{j,k}}^m}{2} \tag{34}$$

where

$$\bar{U}_{z_{j,k}}^m = \frac{U_{j,k}^m + U_{j+1,k}^m}{2}, \quad \bar{V}_{z_{j,k}}^m = \frac{V_{j,k}^m + V_{j,k-1}^m}{2} \tag{35}$$

The horizontal velocity components and the vertical velocity at the free surface are now expressed in terms of the non-hydrostatic pressure.

The non-hydrostatic pressure $q_{j,k}^{m+1}$ is calculated implicitly using the continuity equation (4) discretized in the form

$$\frac{U_{j+1,k}^{m+1} - U_{j,k}^{m+1}}{\Delta x} + \frac{V_{j,k}^{m+1} - V_{j,k-1}^{m+1}}{\Delta y} + \frac{w_{s_{j,k}}^{m+1} - w_{b_{j,k}}^{m+1}}{D_{j,k}^m} = 0 \tag{36}$$

Substitution of (29), (30), and (32) into the continuity equation (36) gives a system of linear algebraic equations

$$\mathrm{PL}_{j,k} q_{j-1,k}^{m+1} + \mathrm{PR}_{j,k} q_{j+1,k}^{m+1} + \mathrm{PB}_{j,k} q_{j,k-1}^{m+1} + \mathrm{PT}_{j,k} q_{j,k+1}^{m+1} + \mathrm{PC}_{j,k} q_{j,k}^{m+1} = Q_{j,k} \tag{37}$$

where the coefficients are computed from the surface elevation and flow depth in the forms of $A_{j,k}$ and $B_{j,k}$ in (31)

$$\mathrm{PL}_{j,k} = \frac{\Delta t}{2\rho \Delta x^2}(-1 + A_{j,k})$$

$$\mathrm{PR}_{j,k} = \frac{\Delta t}{2\rho \Delta x^2}(-1 - A_{j+1,k})$$

$$\mathrm{PB}_{j,k} = \frac{\Delta t}{2\rho \Delta y^2}(-1 + B_{j,k-1})$$

$$\mathrm{PT}_{j,k} = \frac{\Delta t}{2\rho \Delta y^2}(-1 - B_{j,k})$$

$$\mathrm{PC}_{j,k} = \frac{\Delta t}{2\rho \Delta x^2}[(1 + A_{j,k}) + (1 - A_{j+1,k})] + \frac{\Delta t}{2\rho \Delta y^2}[(1 + B_{j,k-1}) + (1 - B_{j,k})] + \frac{2\Delta t}{\rho (D_{j,k}^m)^2} \tag{38}$$

and the forcing vector is given in terms of the velocity gradients

$$Q_{j,k} = -\frac{\tilde{U}_{j+1,k}^{m+1} - \tilde{U}_{j,k}^{m+1}}{\Delta x} - \frac{\tilde{V}_{j,k}^{m+1} - \tilde{V}_{j,k-1}^{m+1}}{\Delta y} - \frac{w_{s_{j,k}}^m + w_{b_{j,k}}^m - 2w_{b_{j,k}}^{m+1}}{D_{j,k}^m} \tag{39}$$

DOI: 10.1002/fld

The Poisson-type equation (37) defines the physics of the non-hydrostatic processes through the non-dimensional parameters, $\Delta x/\Delta y, \Delta x/D_{j,k}, \Delta y/D_{j,k}, A_{j,k}$, and $B_{j,k}$. The scaling parameter $\Delta x/\Delta y$ accounts for the different grid sizes along the x and y directions, while $\Delta x/D_{j,k}$ and $\Delta y/D_{j,k}$ define the scales of the horizontal (non-dispersive) and vertical (dispersive) flows. The key role in the generation and modification of dispersive waves lies in $A_{j,k}$ and $B_{j,k}$, which describe the magnitude of the bottom and free-surface slopes. The vertical component of the flow, important for sustaining dispersive processes, is imparted through the bottom and surface slopes in terms of the horizontal flow components from the boundary conditions (5) and (6). As the ocean bottom and surface slopes start to change abruptly at shelf breaks and around steep seamounts and canyons, the coefficients $A_{j,k}$ and $B_{j,k}$ may strongly influence the solution process. The equation type may even change in the run-up calculation as the water depth $h_{j,k}$ varies from positive to negative across the shoreline and the values of $A_{j,k}$ and $B_{j,k}$ can be greater than unity.

In the implementation, the non-hydrostatic pressure is assigned to be zero at the boundary cells of the computational domain [12]. The matrix equation (37) in the form of $[P]\{q\}=\{Q\}$ provides the non-hydrostatic pressure over the interior cells at each time step. The matrix $[P]$ is non-symmetric, which is solved by the bi-conjugate gradient squared stabilized (Bi-CGSTAB) algorithm with an incomplete lower upper (ILU) preconditioner [23–25]. Once the non-hydrostatic pressure is determined, the horizontal velocity is calculated from (29) and (30) and the bottom and free surface vertical velocities from (32) and (33), respectively. The surface elevation is computed from (12) with the horizontal velocity components from (29) and (30) to complete the non-hydrostatic solution.

3.3. Wet–dry moving boundary condition

For inundation or run-up calculations, special numerical treatments are necessary to describe the moving waterline in the swash zone. The present non-hydrostatic model keeps track of the interface between wet and dry cells using the approach of Kowalik *et al.* [22] that extrapolates the numerical solution from the wet region onto the beach. The non-hydrostatic pressure is set to be zero at the wet cells along the wet–dry interface to conform with the solution scheme of the non-hydrostatic model.

The moving waterline scheme provides an update of the wet–dry interface as well as the associated flow depth and velocity at the beginning of every time step. A marker $\mathrm{CELL}^m_{j,k}$ first updates the wet–dry status of each cell based on the flow depth and surface elevation. If the flow depth $D^m_{j,k}$ is positive, the cell is under water and $\mathrm{CELL}^m_{j,k}=1$, and if $D^m_{j,k}$ is zero or negative, the cell is dry and $\mathrm{CELL}^m_{j,k}=0$. This captures the retreat of the waterline in an ebb flow. The surface elevation along the interface then determines any advancement of the waterline. For flows in the positive x direction, if $\mathrm{CELL}^m_{j,k}$ is dry and $\mathrm{CELL}^m_{j-1,k}$ is wet, $\mathrm{CELL}^m_{j,k}$ is reevaluated as

$$\mathrm{CELL}^m_{j,k}=1 \text{ (wet)} \quad \text{if } \zeta^m_{j-1,k} > -h_{j,k}$$

$$\mathrm{CELL}^m_{j,k}=0 \text{ (dry)} \quad \text{if } \zeta^m_{j-1,k} \leqslant -h_{j,k}$$

If $\mathrm{CELL}^m_{j,k}$ becomes wet, the scheme assigns the flow depth and velocity component at the cell as

$$D^m_{j,k}=\zeta^m_{j-1,k}+h_{j,k}, \quad U^m_{j,k}=U^m_{j-1,k}$$

The marker $\mathrm{CELL}^m_{j,k}$ is then updated for flows in the negative x direction. The same procedures are implemented in the y direction to complete the wet–dry status of the cell. In case the water flows into a new wet cell from multiple directions, the flow depth is averaged.

DOI: 10.1002/fld

Once the wet–dry cell interface is open by setting $\mathrm{CELL}_{j,k}^{m}=1$, the flow depth $D_{j,k}^{m}$ and velocity $(U_{j,k}^{m}, V_{j,k}^{m})$ are assigned to the new wet cell to complete the update of the wet–dry interface at time step m. The surface elevation $\zeta_{j,k}^{m+1}$ and the flow velocity $(U_{j,k}^{m+1}, V_{j,k}^{m+1})$ over the computational domain are obtained through integration of the momentum and continuity equations along with the implicit solution of the non-hydrostatic pressure as outlined in Sections 3.1 and 3.2. The moving waterline scheme is then repeated to update the wet–dry interface at the beginning of the $(m+1)$ time step. This approach remains stable and robust for the non-hydrostatic flows without artificial dissipation mechanisms.

4. RESULTS AND DISCUSSION

We implemented the momentum-conserved advection scheme and the non-hydrostatic formulation to the nonlinear shallow-water model of Kowalik *et al.* [22]. The resulting FORTRAN program, NEOWAVE (Non-hydrostatic Evolution of Ocean WAVE), has a modular structure that allows selection of various numerical schemes in building a hydrostatic or non-hydrostatic model for a specific application. Previous studies have verified and validated the hydrostatic model for wave propagation, transformation, and run-up with analytical solution and laboratory data [3, 11, 22, 26]. This study verifies and validates the non-hydrostatic model through a series of numerical experiments involving solitary wave propagation in a channel, sinusoidal wave transformation over a submerged bar, and solitary wave run-up on a plane beach and a conical island. In addition, we examine the model performance with and without the upwind flux approximation in the wave transformation experiment and with and without the momentum-conserved advection scheme in the two run-up experiments. No filtering is applied in the numerical results presented in this study.

4.1. Solitary wave propagation in a channel

The assumptions on the pressure and vertical velocity distributions in the present non-hydrostatic model are equivalent to those of the classical Boussinesq equations. Since the solitary wave is a solution of the classical Boussinesq equations, the numerical experiment of solitary wave propagation in a channel of constant depth has been a standard test for non-hydrostatic models [12, 15]. The solitary wave should maintain its waveform and celerity through propagation in an inviscid fluid. In the numerical experiment, we consider a 2500 m long and 10 m deep channel with radiation conditions at both ends. The initial condition corresponds to a 2 m high solitary wave at $x=100$ m. The computation uses $\Delta x=\Delta y=1.0$ m, $\Delta t=0.05$ s, and a Manning's roughness coefficient $n=0.0$ for the inviscid flow.

Figure 2 shows the initial solitary wave and the computed waveforms along the channel at 5, 60, 120, and 180 s. The wave height decreases slightly at the very beginning due to the use of an analytical solution as the initial condition. The computed waveform stabilizes with a maximum surface elevation of 1.92 m after $t\approx 5$ s. The horizontal dotted line at $\zeta=1.92$ m indicates that the wave height remains steady for the remainder of the simulation. The computed waveform maintains its symmetry without noticeable trailing waves after propagating for 180 s in the channel. The ability to maintain the solitary waveform derives from the non-hydrostatic terms in the formulation. Numerical experiments with the upwind flux approximation replaced by the second-order scheme or with the momentum-conserved advection scheme turned off yielded very similar results, which

DOI: 10.1002/fld

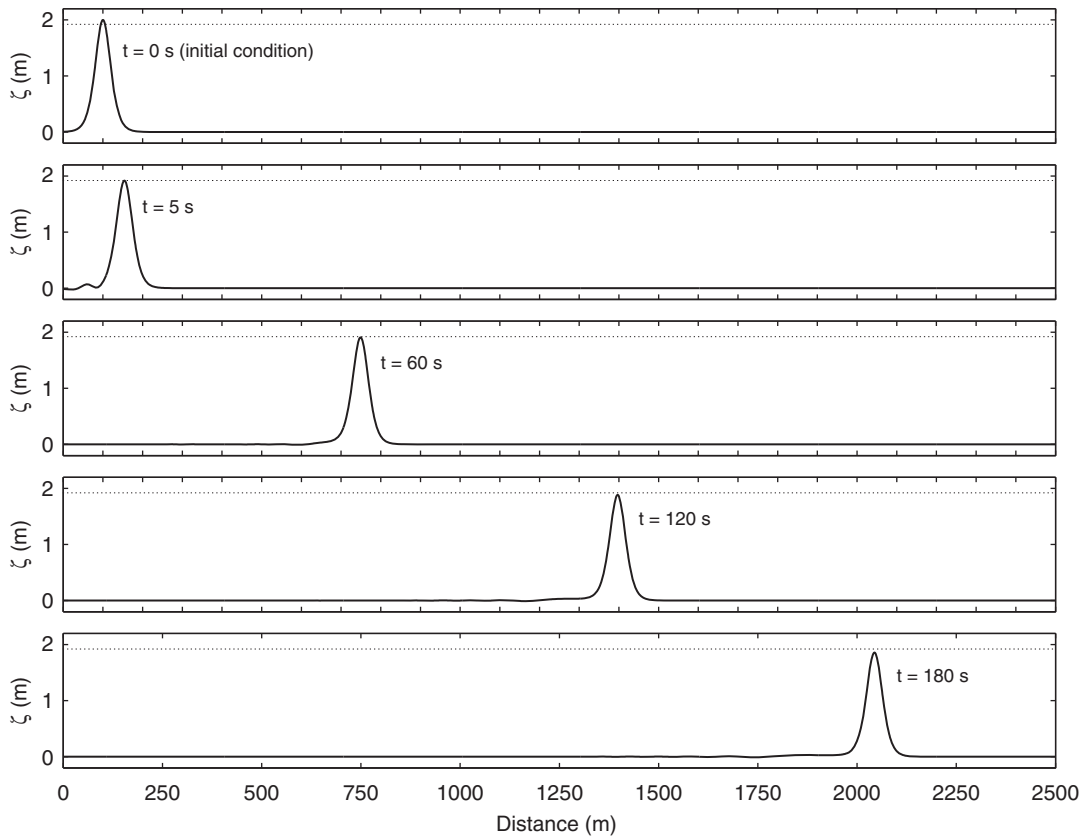

Figure 2. Solitary wave profiles along a channel with constant water depth.

are not presented here for brevity. Refinement of the computational grid, however, can diminish the initial reduction of the wave height, confirming that as a numerical artifact.

4.2. Sinusoidal wave propagation over a bar

Beji and Battjes [27] and Luth *et al.* [28] conducted a laboratory experiment to examine sinusoidal wave propagation over a submerged bar. Figure 3(a) shows the experimental setup in a 37.7 m long, 0.8 m wide, and 0.75 m high wave flume. A hydraulically driven, piston-type random wave generator is located at the left side of the flume and a 1:25 plane beach with coarse material is placed at the right side to serve as a wave absorber. The submerged trapezoidal bar is 0.3 m high with front slope of 1:20 and lee slope of 1:10. The computational domain in Figure 3(b) is 35 m long and 0.4 m deep and is discretized with $\Delta x = \Delta y = 1.25$ cm and $\Delta t = 0.01$ s. Surface roughness is unimportant in this experiment and a Manning's coefficient $n = 0.0$ is used. We consider the test case with the 1 cm incident wave amplitude and 2.02 s wave period that corresponds to the water depth parameter $kh = 0.67$, where k is the wave number. The incident sinusoidal waves are generated at the left boundary and the radiation boundary condition is imposed on the right. The free-surface elevations are recorded at eight gauges over and behind the bar as in the laboratory experiment.

DOI: 10.1002/fld

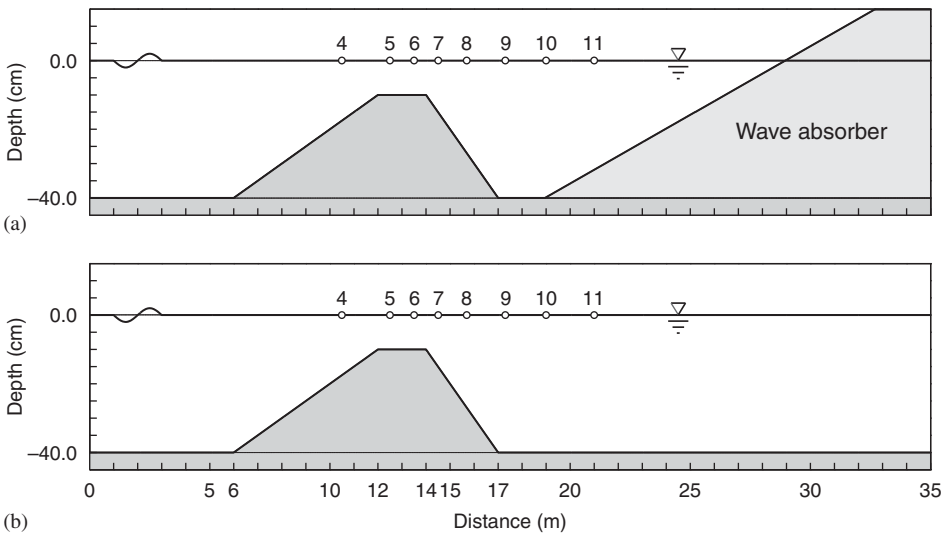

Figure 3. Definition sketch of wave transformation over a submerged bar: (a) laboratory setup and (b) numerical model setup. ○, gauge locations.

Figure 4 shows the computed and recorded waveforms at the eight gauges. The measured data at gauge 4 provide a reference for adjustment of the timing of computed waveforms. The present model with either the upwind flux approximation (13a and 13b) or the second-order scheme (15a and 15b) in the continuity equation reproduces the wave transformation at gauge 4 over the front slope and at gauge 5 immediately behind the front slope. The computed results maintain good agreement with the laboratory data at gauges 6–8 over the crest and the lee slope, where the waveform undergoes significant transformation with high-frequency dispersion. Noticeable discrepancies arise between the computed and recorded waveforms over the flat bottom behind the bar, where the laboratory data from gauges 9–11 show evidence of super-harmonics around a 1 s period. These second-order waves, which correspond to $kh = 1.7$ behind the bar, are well beyond the applicable range of the present non-hydrostatic approximation.

Overall, the upwind flux approximation (13a and 13b) and the second-order scheme (15a and 15b) in the present model provide the same or slightly better results compared with Stelling and Zijlema [12] and Walters [15]. The present and previously computed waveforms are almost identical, when the depth-integrated models are within the applicable range of the non-hydrostatic approximation. The high-frequency waves behind the bar exceed the applicable dispersion range of the depth-integrated formulation. Under these critical conditions, the second-order scheme provides larger wave amplitudes, which can be seen at gauges 7–10, especially at gauge 9. This alludes to the importance of the upwind flux approximation in maintaining numerical stability of the model especially when implemented outside its applicable range.

4.3. Solitary wave run-up on a plane beach

Hall and Watts [29], Li and Raichlen [30], and Synolakis [31] conducted series of laboratory experiments for solitary wave transformation and run-up on a plane beach. These experiments,

DOI: 10.1002/fld

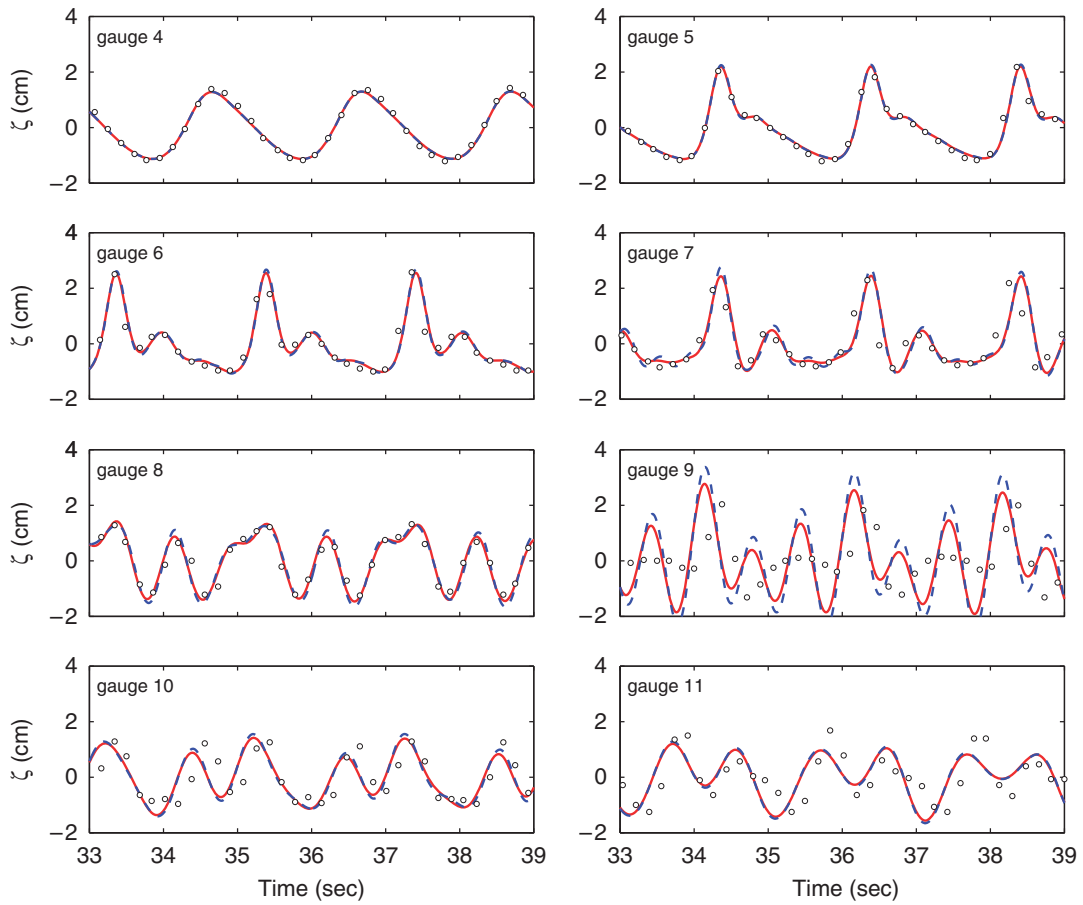

Figure 4. Comparison of computed and measured free-surface elevations over and behind a submerged bar. ○, laboratory data of Beji and Battjes [27]; —— (red), non-hydrostatic model with upwind flux scheme; - - - - (blue), second-order scheme.

which cover a wide range of non-breaking and breaking waves, have become an accepted test case for validation of run-up models [20, 30, 32, 33]. Figure 5 provides a schematic of the experiments with A indicating the incident solitary wave height, β the beach slope, and R the run-up. Following Titov and Synolakis [32], the solitary wave is initially at half wavelength from the toe of the beach in the numerical experiment. The approximate wavelength of a solitary wave is given by

$$L = \frac{2}{k} \operatorname{arccosh}\left(\sqrt{\frac{1}{0.05}}\right) \tag{40}$$

in which the wave number $k = \sqrt{3A/4h^3}$. In the numerical experiment, we use $\Delta x/h = 0.125$ and a Courant number $Cr = 0.2$. Surface roughness becomes important for run-up over gentle slopes and a Manning's coefficient $n = 0.01$ describes the surface condition of the smooth glass beach in the laboratory experiments.

DOI: 10.1002/fld

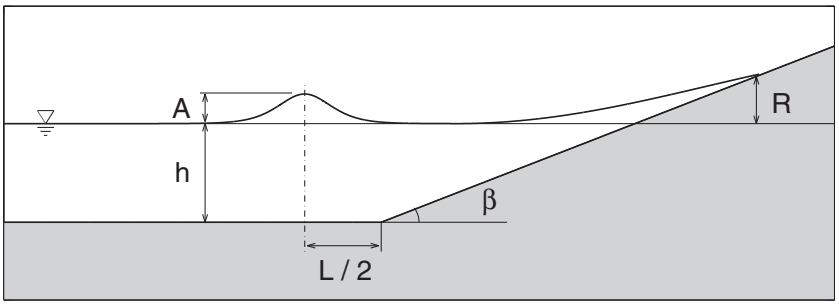

Figure 5. Definition sketch of solitary wave run-up on a plane beach.

Titov and Synolakis [32] present a series of surface profiles with a beach slope of 1:19.85 and solitary wave heights of up to $A/h=0.3$. Initial testing with this experiment reiterates and furthers the findings from the wave transformation experiment in Section 4.2. The upwind flux approximation of the surface elevation is essential in maintaining stability of the depth-integrated non-hydrostatic model, especially when flow discontinuities associated with breaking waves and hydraulic jumps develop. The second-order scheme produces spurious waves near the discontinuity that lead to development of instabilities in most of the tests. As a result, we use the upwind flux approximation in the model throughout this test case and examine the treatment of the advective terms in the momentum equations by presenting results with and without the momentum-conserved advection approximation (20)–(25b). When this scheme is off, the advective terms are computed directly from (14).

Figure 6 shows a comparison of the measured profiles with the two sets of numerical results for the test case with the solitary wave height $A/h=0.3$. The laboratory data show wave breaking between $t(g/h)^{1/2}=20$ and 25 as the solitary wave reaches the beach and development of a hydraulic jump at $t(g/h)^{1/2}=50$ when the water recedes from the beach. Both numerical solutions show very good agreement with the laboratory data as the solitary wave shoals to its maximum height at $t(g/h)^{1/2}=20$. The momentum-conserved advection scheme reproduces the subsequent wave breaking without the use of predefined criteria and matches the surface elevation and run-up on the beach. Without the momentum-conserved advection, the model cannot reproduce the surface profile at $t(g/h)^{1/2}=25$ immediately after wave breaking and underestimates the surface elevation on the beach and eventually the run-up. Both solutions describe the surface elevation reasonably well during the drawdown process. A minor discrepancy on the location of the hydraulic jump occurs around the peak of the return flow at $t(g/h)^{1/2}=55$. The finite volume model of Wei *et al.* [33] also produces a similar discrepancy with the laboratory data. This may attribute to the three-dimensional flow structure that is not amendable to depth-integrated solutions. The agreement resumes as the speed of the return flow decreases demonstrating the resilience of the model.

Figure 7 shows the computed and measured run-up R/h as a function of the solitary wave height A/h for beach slopes of 1:5.67, 1:15, and 1:19.85. The measured data show a bilinear distribution with the two branches representing the non-breaking and breaking regimes separated by a transition. Figure 7(a) shows good agreement of the two solutions with the laboratory data for non-breaking and breaking wave run-up on the 1:5.67 slope. This steep slope most likely produces surging wave breakers that are amendable to non-hydrostatic models without special treatments to the momentum equations. Wave breaking becomes more energetic and the resulting surface elevation

DOI: 10.1002/fld

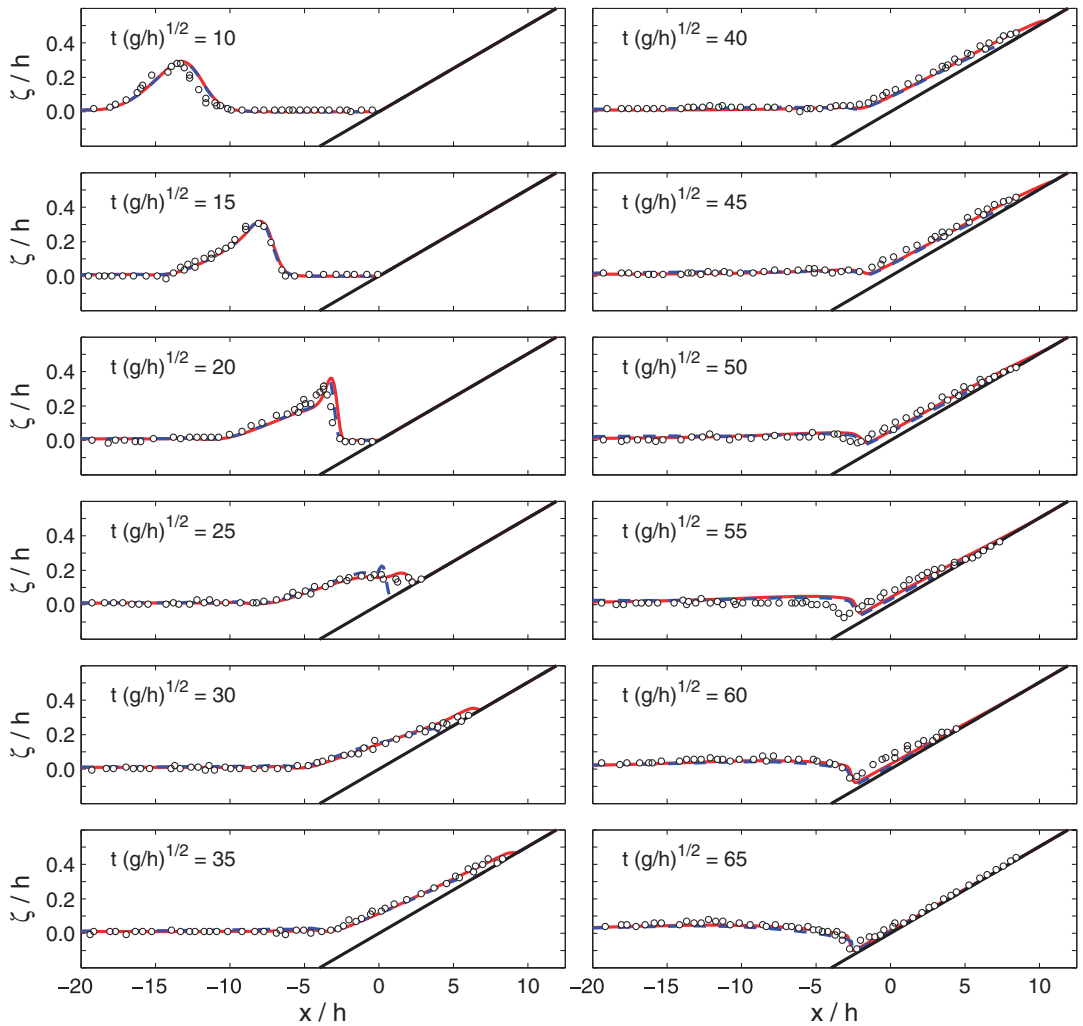

Figure 6. Surface profiles of a solitary wave on a 1:19.85 plane beach with $A/h=0.3$. ∘, laboratory data of Titov and Synolakis [32]; —— (red), non-hydrostatic model with momentum-conserved advection; - - - - (blue), without momentum-conserved advection.

becomes discontinuous as the beach slope decreases. In Figure 7(b) and (c), the computed run-up from the momentum-conserved advection scheme shows excellent agreement with the laboratory data for both non-breaking and breaking waves. Without the momentum conservation, the solution reproduces the run-up in the non-breaking and transition regimes, but underestimates the measured run-up for breaking waves with $A/h>0.1$. This shows that implementation of the momentum-conserved advection in a non-hydrostatic model can capture discontinuous flows associated with energetic wave breaking and describe the subsequent run-up on the beach for the full range of solitary wave height.

DOI: 10.1002/fld

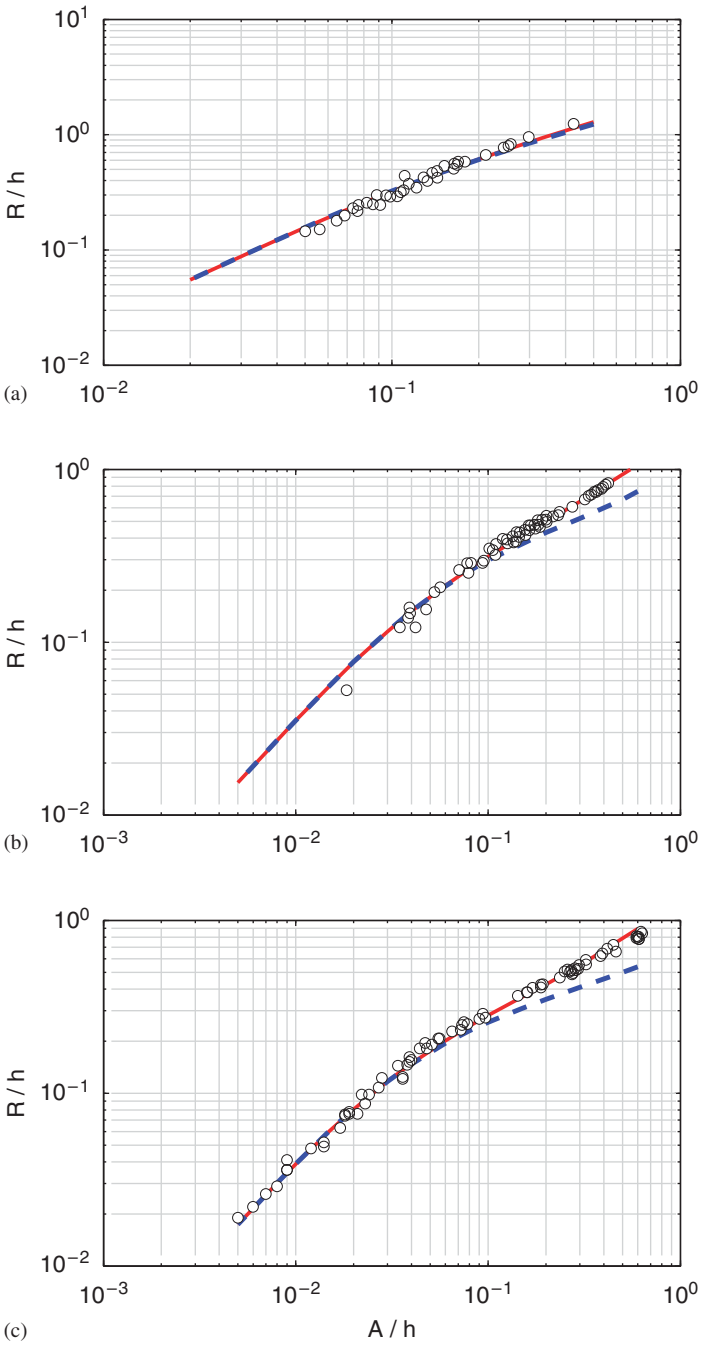

Figure 7. Solitary wave run-up on a plane beach as a function of incident wave height: (a) 1/5.67 [29]; (b) 1/15 [30]; and (c) 1/19.85 [31]. ∘, laboratory data; —— (red), non-hydrostatic model with momentum-conserved advection; - - - - (blue), without momentum-conserved advection.

DOI: 10.1002/fld

4.4. Solitary wave run-up on a conical island

Briggs *et al.* [34] conducted a large-scale laboratory experiment to investigate solitary wave run-up on a conical island. The collected data have become a standard for validation of run-up models [4, 6, 19, 20, 33]. Figure 8 shows a schematic of the experiment. The basin is 25 m long and 30 m wide. The circular island has the shape of a truncated cone with diameters of 7.2 m at the base and 2.2 m at the crest. The island is 0.625 m high and has a side slope of 1:4. The surface of the island and basin has a smooth concrete finish. A 27.4 m long directional spectral wave maker, which consists of 61 paddles, generates solitary waves for the experiment. Wave absorbers at the three sidewalls reduce reflection.

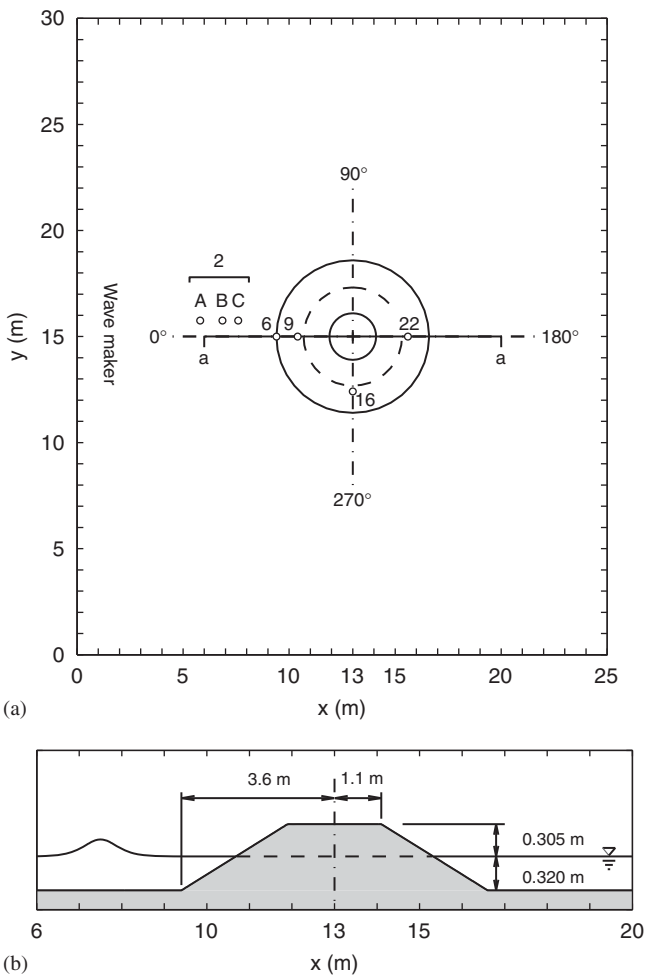

Figure 8. Schematic sketch of the conical island experiment: (a) plane view and (b) side view. ○, gauge locations.

DOI: 10.1002/fld

The experiment covers the water depths $h=0.32$ and 0.42 m and the solitary wave heights $A/h=0.05, 0.1$, and 0.2. The present study considers the smaller water depth $h=0.32$ m, which provides a more critical test case for the model. In the computation, the solitary wave is generated from the left boundary with the measured initial wave heights of $A/h=0.045$, 0.096, and 0.181. These measured wave heights in the laboratory experiment, instead of the target wave heights $A/h=0.05, 0.1$, and 0.2, better represent the recorded data at gauge 2 and thus the incident wave conditions to the conical island. The radiation condition is imposed at the lateral boundaries to model the effects of the wave absorbers. We use $\Delta x=\Delta y=5$ cm, $\Delta t=0.01$ s, and a Manning's roughness coefficient $n=0.016$ for the smooth concrete finish. Since wave breaking occurred during the laboratory experiment, we use the upwind flux approximation in the computation to model the processes.

The solution obtained with the momentum-conserved advection scheme provides an illustration of the solitary wave transformation around the conical island. Figure 9 shows the results when the wave reaches the maximum elevation on the front face of the island and 2 s afterward. Because the celerity increases with the wave height, the arrival time of the solitary wave is 1.4 s apart for the wave height range considered. The three test cases show refraction and trapping of the solitary wave over the island slope. The left panels of Figure 10 show that the trapped waves from the two sides superpose with the diffracted wave at the lee side of the island. Wave breaking occurs locally for $A/h=0.096$ and everywhere around the island for $A/h=0.181$ [6]. This reduces the subsequent run-up on the lee side of the island. The right panels show the free surface 2 s later when the trapped waves have passed each other and continue to wrap around to the front. Munger and Cheung [35] reported similar trapped waves around the Hawaiian Islands generated by the 2006 Kuril Islands tsunami that lasted for two days.

The free surface is rather smooth with indistinguishable frequency dispersion before the wave wraps around the island. As the solitary wave travels down the basin, high-frequency dispersive waves become evident around the island especially on the lee side. The test case with $A/h=0.181$ provides a vivid depiction of the generation and propagation of the dispersive waves. Figures 9(c) and 10(c) show the generation of the first group of dispersive waves as the trapped waves wrap around the island and collide on the lee side. After the collision, the second group of dispersive waves is generated due to energy leakage from the two trapped waves that continue to wrap around to the front. The interaction of the first and second groups of dispersive waves generates a mesh-like wave pattern behind the island. These high-frequency dispersive waves provide an explanation for the 3–5 min edge waves recorded on the south shore of Oahu after the 2006 Kuril Islands tsunami that a nonlinear shallow-water model cannot reproduce even with a 10 m computational grid [36].

A number of gauges recorded the transformation of the solitary wave around the conical island. Figure 11 shows the time series of the solutions with and without the momentum-conserved advection scheme and the measured free-surface elevations at selected gauges. With reference to Figure 8, gauges 2 and 6 are located in front of the island and 9, 16, and 22 are placed just outside the still waterline around the island. These gauges provide sufficient coverage of the representative wave conditions in the experiment. The measured data at gauge 2 provide a reference for adjustment of the timing of the computed waveforms. Both solutions show excellent agreement with the measured time series including the depression following the leading wave that was not adequately reproduced in previous studies. The momentum-conserved advection scheme reasonably describes the phase of the peak, but slightly overestimates the leading wave amplitude at gauges 9 and 22 as the wave height increases. Without the momentum conservation, the model

DOI: 10.1002/fld

generally reproduces the leading wave amplitude except at gauge 22 with $A/h=0.181$, where the model fails to fully capture the energetic breaking wave on the lee side of the island. This reiterates the importance of the momentum-conserved advection scheme in capturing breaking waves.

Figure 12 shows comparisons of the measured and computed inundation and run-up around the conical island. Both solutions from the present model are almost identical and show good agreement with the laboratory data. The momentum-conserved advection produces better estimations at the lee flank of island around 90−160°, where the run-up is lowest. For the results presented in

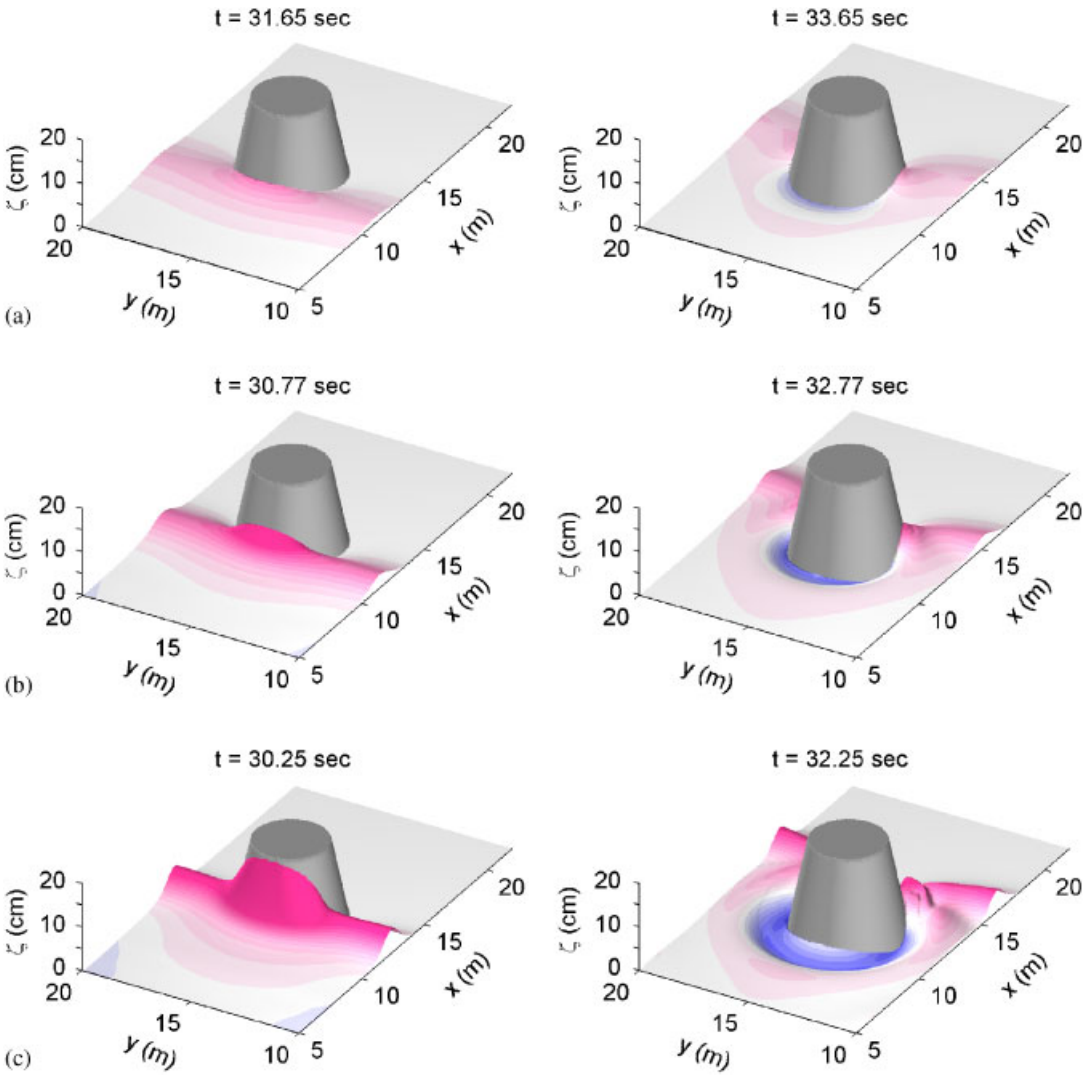

Figure 9. Wave transformation in front of the conical island: (a) $A/h=0.045$; (b) $A/h=0.096$; and (c) $A/h=0.181$.

DOI: 10.1002/fld

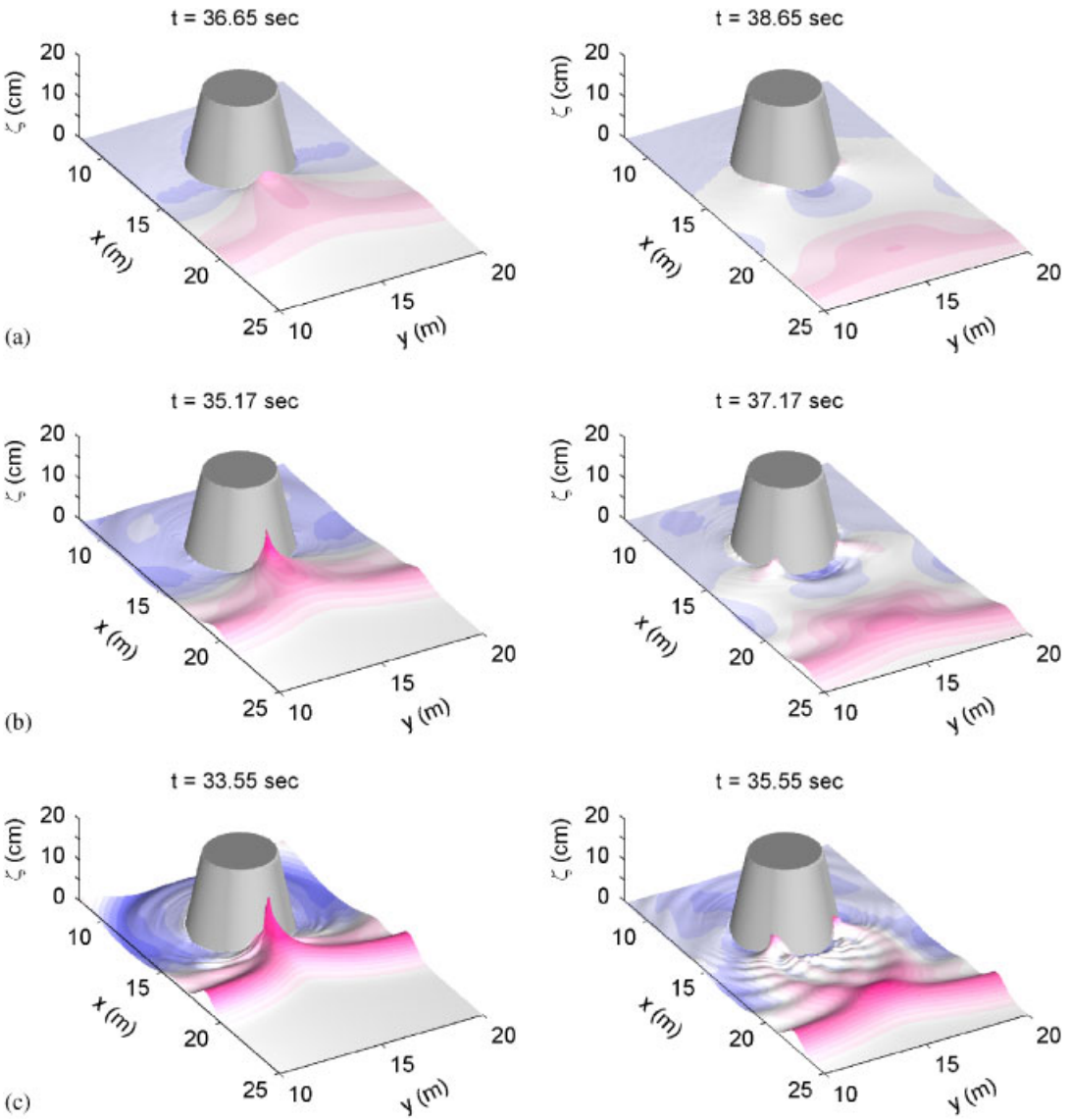

Figure 10. Wave transformation on the lee side of the conical island: (a) $A/h=0.045$; (b) $A/h=0.096$; and (c) $A/h=0.181$.

Figures 11 and 12, both solutions are comparable or slightly better than the extended Boussinesq solutions of Chen *et al.* [19] and Lynett *et al.* [20] that use empirical relations with adjustable coefficients to describe wave breaking. Most of the previous studies neglected friction in this numerical experiment [4, 6, 19, 20]. We also tested the model with $n=0.0$ and obtained very similar results as $n=0.016$. As pointed out in Liu *et al.* [4], the computed results are not sensitive to the surface roughness coefficient due to the steep 1:4 slope of the conical island. The overall agreement

DOI: 10.1002/fld

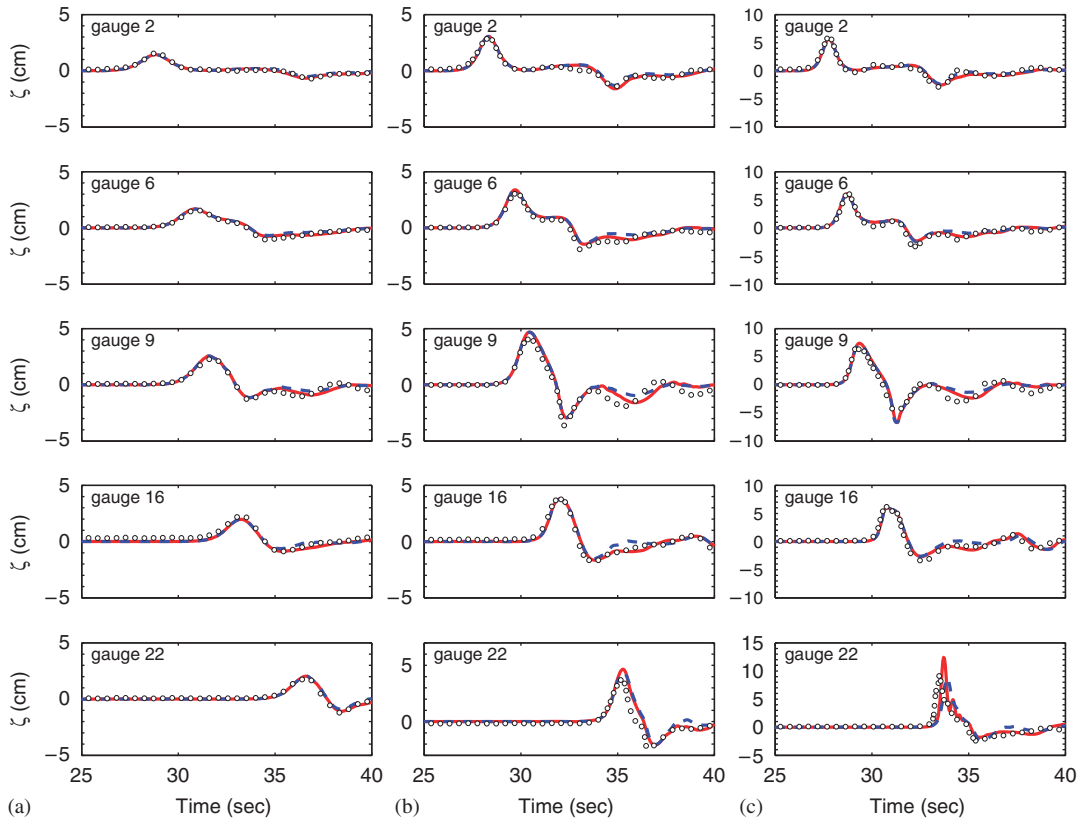

Figure 11. Time series of surface elevations at gauges around a conical island: (a) $A/h=0.045$; (b) $A/h=0.096$; (c) $A/h=0.181$. ∘, laboratory data from Briggs *et al.* [34]; —— (red), non-hydrostatic with momentum-conserved advection; - - - - (blue), without momentum-conserved advection.

between the computed results and laboratory data indicates the capability of the present model to estimate wave transformation, breaking, and inundation in the two horizontal dimensions.

Numerical models for tsunami flood hazards need to deal with wave dispersion in basin-wide propagation and flow discontinuities due to wave breaking near shore, but at the same time, must be articulate, stable in dealing with flows over complex topography, and efficient for large computational problems. The present depth-integrated, non-hydrostatic model with a semi-implicit scheme appears to satisfy these requirements for practical application. The computing time depends on the grid size and number of iterations in the non-hydrostatic solver. For the results presented in this paper, the computing time is about 2–2.5 times in comparison with the hydrostatic solution. The turn-around time can be reduced through parallel computing. The model results are very stable and do not show any spurious oscillations even with the most energetic wave-breaking conditions. Among the existing dispersive models, the present model utilizes the simplest dispersive term, which is only the first derivative of the non-hydrostatic pressure. This would be the reason for the stability achieved by the present model without any spatial filtering of the solution. The use of the upwind flux approximation of the surface elevation in the continuity and momentum

DOI: 10.1002/fld

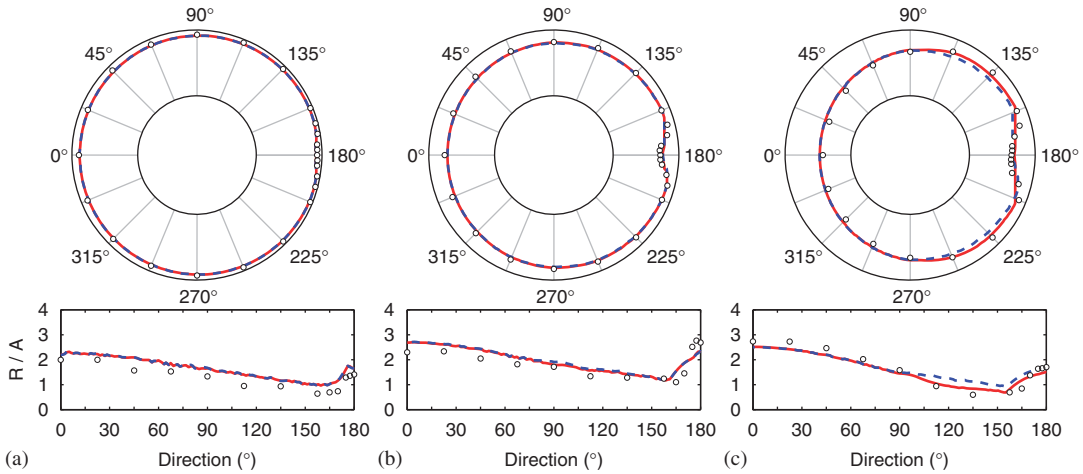

Figure 12. Inundation and run-up around a conical island: (a) $A/h=0.045$; (b) $A/h=0.096$; (c) $A/h=0.181$. ○, laboratory data from Briggs *et al.* [34]; —— (red), non-hydrostatic model with momentum-conserved advection; - - - - (blue), without momentum-conserved advection.

equations further improves the model stability and becomes essential with wave breaking. This portends well for the implementation of the present non-hydrostatic model with realistic topography as already demonstrated by Kowalik *et al.* [22] for the hydrostatic part of the model. Future applications include tsunami inundation mapping and forecasting along with the inverse algorithm [37–39].

5. CONCLUSIONS

This paper describes a depth-integrated, non-hydrostatic model for wave propagation, transformation, breaking, and run-up. The formulation decomposes the pressure into hydrostatic and non-hydrostatic components and introduces a vertical velocity in response to the non-hydrostatic pressure. The hydrostatic component is equivalent to a nonlinear shallow-water model with an explicit scheme, and an implicit scheme provides the non-hydrostatic pressure through the three-dimensional continuity equation. A unique feature of the model is the use of an upwind flux approximation, which extrapolates the free-surface elevation instead of the flow depth, in the computation of the continuity equation and the momentum-conserved advection.

The present depth-integrated dispersive model is equivalent to those based on the classical Boussinesq equations for weakly dispersive waves. The upwind flux approximation in the continuity equation has little effect on wave propagation, while it is essential for providing stable solutions when energetic wave breaking occurs. The momentum-conserved advection scheme captures flow discontinuities associated with breaking waves as bores and hydraulic jumps and reproduces the results in the plane-beach and conical island run-up experiments. The model can describe wave breaking over steep slope without the momentum-conserved advection, but underestimates the run-up on gentle slope, when breaking becomes more energetic.

DOI: 10.1002/fld

The present model provides comparable results with existing depth-integrated, non-hydrostatic models in wave propagation and transformation, and similar or slightly better estimates than extended Boussinesq models in wave transformation and run-up in the test cases considered. In contrast to Boussinesq-type models, the present model does not require empirical relations or dissipation coefficients for wave breaking and the results remain stable without artificial filtering. The semi-implicit scheme is efficient for large computational problems in practical applications. The proposed non-hydrostatic formulation provides a useful scheme to adapt existing nonlinear shallow-water models for breaking and weakly dispersive waves and extend their usefulness in modeling and assessment of tsunami flood hazards.

ACKNOWLEDGEMENTS

This publication is funded in part by a grant/cooperative agreement from the National Oceanic and Atmospheric Administration (NOAA), Project No. R/EP-32, which is sponsored by the University of Hawaii Sea Grant College Program, School of Ocean and Earth Science and Technology (SOEST), under Institutional Grant No. NA05OAR4171048 from NOAA Office of Sea Grant, Department of Commerce. The National Tsunami Hazard Mitigation Program and Hawaii State Civil Defense provided additional support through the project 'Tsunami Inundation Map for Hawaii'. The authors would like to thank Prof. GS Stelling for his input on the momentum-conserved advection scheme and an anonymous reviewer for the thorough review and constructive remarks on the paper. The views expressed herein are those of the authors and do not necessarily reflect the views of NOAA and any of its sub-agencies. UNIHI-SEAGRANT-JC-08-03. SOEST Contribution No. 7466.

REFERENCES

1. Shuto N, Goto C. Numerical simulation of tsunami run-up. *Coastal Engineering of Japan* 1978; **21**(1):13–20.
2. Mader CL, Curtis G. Modeling Hilo, Hawaii tsunami inundation. *Science of Tsunami Hazards* 1991; **9**(1):85–94.
3. Kowalik Z, Murty TS. Numerical simulation of two-dimensional tsunami runup. *Marine Geodesy* 1993; **16**(2): 87–100.
4. Liu PLF, Cho YS, Briggs MJ, Kanoglu U, Synolakis CE. Runup of solitary wave on a circular island. *Journal of Fluid Mechanics* 1995; **302**:259–285.
5. Imamura F. Review of tsunami simulation with a finite difference method. In *Long-wave Runup Models*, Yeh H, Liu P, Synolakis C (eds). World Scientific: Singapore, 1996; 25–42.
6. Titov VV, Synolakis CE. Numerical modeling of tidal wave runup. *Journal of Waterway*, *Port*, *Coastal*, *and Ocean Engineering* 1998; **124**(4):157–171.
7. Stelling GS, Duinmeijer SPA. A staggered conservative scheme for every Froude number in rapidly varied shallow water flows. *International Journal for Numerical Methods in Fluids* 2003; **43**(12):1329–1354.
8. Dodd N. Numerical model of wave run-up, overtopping, and regeneration. *Journal of Waterway*, *Port*, *Coastal*, *and Ocean Engineering* 1998; **124**(2):73–81.
9. Zhou JG, Causon DM, Mingham CG, Ingram DM. The surface gradient method for the treatment of source terms in the shallow-water equations. *Journal of Computational Physics* 2001; **168**(1):1–25.
10. Wu YY, Cheung KF. Explicit solution to the exact Riemann problem and application in nonlinear shallow-water equations. *International Journal for Numerical Methods in Fluids* 2008; **57**(11):1649–1668.
11. Horrillo J, Kowalik Z, Shigihara Y. Wave dispersion study in the Indian Ocean tsunami of December 26, 2004. *Marine Geodesy* 2006; **29**(1):149–166.
12. Stelling GS, Zijlema M. An accurate and efficient finite-difference algorithm for non-hydrostatic free-surface flow with application to wave propagation. *International Journal for Numerical Methods in Fluids* 2003; **43**(1):1–23.
13. Casulli V. A semi-implicit finite difference method for non-hydrostatic free surface flows. *International Journal for Numerical Methods in Fluids* 1999; **30**(4):425–440.
14. Keller HB. A new difference scheme for parabolic problems. In *Numerical Solutions of Partial Differential Equations*, *II*, Hubbard B (ed.). Academic Press: New York, 1971; 327–350.

DOI: 10.1002/fld

15. Walters RA. A semi-implicit finite element model for non-hydrostatic (dispersive) surface waves. *International Journal for Numerical Methods in Fluids* 2005; **49**(7):721–737.
16. Peregrine DH. Long waves on a beach. *Journal of Fluid Mechanics* 1967; **27**(4):815–827.
17. Zijlema M, Stelling GS. Efficient computation of surf zone waves using the nonlinear shallow water equations with non-hydrostatic pressure. *Coastal Engineering* 2008; **55**(10):780–790.
18. Madsen PA, Sørensen OR, Schäffer HA. Surf zone dynamics simulated by a Boussinesq type model. Part I. Model description and cross-shore motion of regular waves. *Coastal Engineering* 1997; **32**(4):255–287.
19. Chen Q, Kirby JT, Dalrymple RA, Kennedy AB, Chawla A. Boussinesq modeling of wave transformation, breaking, and runup. II: 2D. *Journal of Waterway, Port, Coastal, and Ocean Engineering* 2000; **126**(1):48–56.
20. Lynett PJ, Wu TR, Liu PLF. Modeling wave runup with depth-integrated equations. *Coastal Engineering* 2002; **46**(2):89–107.
21. Mader CL. *Numerical Modeling of Water Waves*. CRC Press: New York, 1993.
22. Kowalik Z, Knight W, Logan T, Whitmore P. Numerical modeling of the global tsunami: Indonesian tsunami of 26 December 2004. *Science of Tsunami Hazards* 2005; **23**(1):40–56.
23. Van der Vorst HA. Bi-CGSTAB: a fast and smoothly converging variant of Bi-CG for the solution of nonsymmetric linear systems. *SIAM Journal on Scientific and Statistical Computing* 1992; **13**(2):631–644.
24. Van der Vorst HA. Iterative solution methods for certain sparse linear systems with a non-symmetric matrix arising from PDE-problems. *Journal of Computational Physics* 1981; **44**(1):1–19.
25. Ferziger JH, Perić M. *Computational Methods for Fluid Dynamics*. Springer: Berlin, 2002.
26. Kowalik Z, Murty TS. *Numerical Modeling of Ocean Dynamics*. World Scientific: Singapore, 1993.
27. Beji S, Battjes JA. Experimental investigation of wave propagation over a bar. *Coastal Engineering* 1993; **19**(1–2):151–162.
28. Luth HR, Klopman G, Kitou N. Project 13G: kinematics of waves breaking partially on an offshore bar; LDV measurements for waves with and without a net onshore current. *Technical Report H1573*, Delft Hydraulics, 1994.
29. Hall JV, Watts JW. Laboratory investigation of the vertical rise of solitary waves on impermeable slopes. *Technical Memo No. 33*, Beach Erosion Board, U.S. Army Corps of Engineers, 1953.
30. Li Y, Raichlen F. Non-breaking and breaking solitary wave run-up. *Journal of Fluid Mechanics* 2002; **456**:295–318.
31. Synolakis CE. The runup of solitary waves. *Journal of Fluid Mechanics* 1987; **185**:523–545.
32. Titov VV, Synolakis CE. Modeling of breaking and nonbreaking long-wave evolution and runup using VTCS-2. *Journal of Waterway, Port, Coastal, and Ocean Engineering* 1995; **121**(6):308–316.
33. Wei Y, Mao XZ, Cheung KF. Well-balanced finite-volume model for long-wave runup. *Journal of Waterway, Port, Coastal, and Ocean Engineering* 2006; **132**(2):114–124.
34. Briggs MJ, Synolakis CE, Harkins GS, Green DR. Laboratory experiments of tsunami runup on a circular island. *Pure and Applied Geophysics* 1995; **144**(3/4):569–593.
35. Munger S, Cheung KF. Resonance in Hawaii waters from the 2006 Kuril Islands tsunami. *Geophysical Research Letters* 2008; **35**(7):L07605. DOI: 10.1029/2007GL032843.
36. Bricker JD, Munger S, Pequignet C, Wells JR, Pawlak G, Cheung KF. ADCP observations of edge waves off Oahu in the wake of the November 2006 Kuril Island tsunami. *Geophysical Research Letters* 2007; **34**(23):L23617. DOI: 10.1029/2007GL032015.
37. Wei Y, Cheung KF, Curtis GD, McCreery CS. Inverse algorithm for tsunami forecasts. *Journal of Waterway, Port, Coastal, and Ocean Engineering* 2003; **129**(2):60–69.
38. Yamazaki Y, Wei Y, Cheung KF, Curtis GD. Forecast of tsunamis generated at the Japan–Kuril–Kamchatka source region. *Natural Hazards* 2006; **38**(3):411–435.
39. Sánchez A, Cheung KF. Tsunami forecast using an adaptive inverse algorithm for the Peru–Chile subduction zone. *Geophysical Research Letters* 2007; **34**(13):L13605. DOI: 10.1029/2007GL030158.